

## Research Article

Sayyed Ahmad Abtahi, Mohsen Maddahali\*, and Ahmad Bakhtafrouz

# Spin photonic topological metasurface based on kagome lattice and leaky-wave application

**Abstract:**

The emerging field of topological metasurfaces offers unique advantages, particularly in robustness against backscattering in low-profile structures. The lattice configuration of these structures significantly influences the ability to achieve sharp turns in the propagation path. One of the most studied lattices in condensed matter physics is the kagome lattice, characterized by its hexagonal Brillouin zone, which displays a Dirac cone in its dispersion diagram. Previous research on kagome lattices in photonic topological insulators has primarily focused on valley types of insulators. This article introduces a spin topological metasurface based on the kagome lattice and its unit cell, enabling a broad range of sharp turns and propagation paths. The unit cell is compared to its hexagonal and 60-degree rhombic counterparts, and a parametric study of its dimensions is conducted. As a result of this research, a new X-band leaky-wave antenna designed in the kagome lattice with an armchair arrangement interface has been developed. This antenna provides two forward and two backward beams, each pair achieving an approximately 50-degree scan within the 8.8 to 11.1 GHz bandwidth.

**Keywords:** Topological metasurface; Spin PTI; Leaky wave antenna; Kagome lattice

## 1 Introduction

Topological metasurfaces are emerging in this decade as part of the third generation of metasurfaces[1].

**Sayyed Ahmad Abtahi**, Department of Electrical and Computer Engineering, Isfahan University of Technology, Isfahan 84156-83111, Iran, E-mail: abtahi.a@ec.iut.ac.ir; <https://orcid.org/0009-0002-7631-8616>

**\*Corresponding author: Mohsen Maddahali**, Department of Electrical and Computer Engineering, Isfahan University of Technology, Isfahan 84156-83111, Iran, E-mail: maddahali@iut.ac.ir; <https://orcid.org/0000-0001-9839-624X>

**Ahmad Bakhtafrouz**, Department of Electrical and Computer Engineering, Isfahan University of Technology, Isfahan 84156-83111, Iran, E-mail: bakhtafrouz@iut.ac.ir; <https://orcid.org/0000-0002-6496-9967>

They exhibit unique characteristics, such as immunity to backscattering during sharp turns and resilience against manufacturing defects[2]. These structures are part of photonic topological insulators (PTIs), classified into two groups based on whether time-reversal symmetry is preserved or broken. The first group is called Chern PTIs, which consist of photonic crystals made from ferrite rods arranged in a square[3] or honeycomb lattice[4]. Time-reversal symmetry is broken by applying a static magnetic field. Conversely, the second group is distinctly categorized into two types of valley or spin PTIs. This classification is achieved through the breaking of inversion symmetry[5] and electromagnetic duality[6], respectively, which facilitates propagation in two distinct opposing directions.[7].

In the spin PTIs, the quantum spin Hall effect is emulated using electromagnetic duality, characterized by the condition ( $\bar{\epsilon} = \bar{\mu}$ ), in spin-degenerate metamaterials. This setup can lead to either fourfold [6] or twofold [8] degeneracies at the K and K' symmetry points within the irreducible Brillouin zone. Consequently, by enforcing bi-anisotropy, this degeneracy is broken, resulting in the emergence of a non-trivial bandgap [9]. Spin topological metasurfaces are designed on honeycomb[5, 6] and 60-degree[10] and 30-degree[11] rhombic lattices. It is important to note that although the waves propagating in the spin topological metasurfaces are line waves, these structures are distinct from dual impedance metasurfaces.[12–15]. The wave propagating in dual impedance metasurfaces lacks topological protection and will scatter at sharp bends.[16].

In addition to guiding waves, these structures also have been used as leaky wave antennas[11, 17–20]. In [19], the authors utilized spin topological metasurfaces based on a honeycomb lattice arranged in a zigzag pattern. However, the propagation through this zigzag configuration leads to coupling between the radiating elements, resulting in a non-practical radiation pattern. In [11], the coupling problem was addressed using a 30-degree rhombic lattice. However, this lattice structure has a gap in the edge modes, which are situ-

ated in the slow wave region. As a result, the 30-degree rhombic structure is not suitable for waveguiding applications.

This article presents a spin topological metasurface that utilizes a kagome lattice configuration. It begins by detailing the characteristics of the corresponding unit cell and observing the unidirectional propagation of each pseudospin, noting its robustness during sharp turns. Following this, a parametric study is conducted to determine optimal dimensions for operation in X-band frequencies. Drawing inspiration from the results of [21], which focused on the armchair arrangement, the interface line is designed in an armchair configuration for use in a leaky-wave antenna application.

The proposed leaky-wave antenna is designed to radiate two beams forward and two beams backward simultaneously. It operates at a frequency range of 8.8 to 11.1 GHz, allowing for a 50-degree scan for backward beams and a 47-degree scan for forward beams. The simulations conducted using Ansys HFSS have been validated by repeating them in CST Studio. Unfortunately, there are no experimental results available, as the project did not receive funding.

## 2 kagome lattice metasurface characteristics

The kagome lattice is interested in condensed matter physics for inclusion of Dirac cone, flat band and Van Hove singularity [22, 23]. The non-triviality of the lattice has been proven for electronic structures [24] and many valley topological photonic crystals has been proposed based on the lattice [25–32].

Despite mentioned hilarious efforts, there was no low profile spin PTI on Kagome lattice to the best of our knowledge. The method of using EM duality in complementary cell to achieve a low profile spin PTI introduced in [6], for the first time, features a hexagonal unit cell shown in Fig.1(a). Inspired by the hexagonal Brillouin zone of a the hexagonal lattice, a 60-degree rhombic unit cell (Fig.1(b)) with a similar Brillouin zone has been introduced [10], and its non-triviality has been proven [8]. The kagome lattice is another structure that exhibits a hexagonal Brillouin zone [33], which will be constructed using the presented unit cell shown in Fig.1(c).

In the following, the dispersion diagram of kagome cell calculated and compared with the 60-degree rhombic cell. Also, the dispersion diagram of one ribbon of each

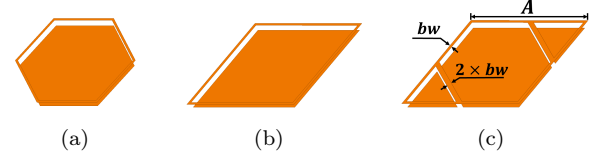


**Fig. 1:** (a) The proposed hexagonal unit cell of the honeycomb lattice, which has been introduced in [6] in zigzag arrangement, (b) the proposed 60-degree rhombic unit cell which has been introduced in [10] and (c) the proposed kagome unit cell which is introduced in this paper. The period length and border width are marked by  $A$  and  $bw$ , respectively.

mentioned cell in Fig.1 determined to observe the edge mode presence and behavior. After that a parametric study on the dimensions of the kagome cell has been conducted, to find appropriate design of the structure in the X-band frequencies.

### 2.1 Dispersion diagram

The period length and border width are set to 20 mm and 0.433 mm, respectively, to facilitate a direct comparison with the 60-degree rhombic unit cell described in [10]. Additionally, the substrate has been selected as Rogers/Duroid 5880, which has a thickness of 1.57 mm and a permittivity of 2.2.

The 3D dispersion of the 60-degree rhombic and kagome unit cells is illustrated in Fig.2(a) and (b), which demonstrate the degeneracy of the bands and the presence of a complete bandgap between them. Notably, the first bandgap of the kagome unit cell is significantly wider than that of the 60-degree rhombic unit cell. Additionally, the dispersion diagram of the irreducible Brillouin zone (IBZ) for the kagome unit cell is shown in Fig.2(c), which aligns with the 3D dispersion diagram presented in Fig.2(b).

The initial indication of the topological nature of the kagome unit cell comes from the double degeneracy of the bands, similar to that described in [6]. To provide further evidence, the dispersion diagrams for one ribbon from each cell, as shown in Fig. 1, have been calculated. The results are presented in Figs. 2(d) to 2(f). These results demonstrate the presence of a Dirac cone for the edge modes of both the zigzag and kagome ribbons, which is absent in the 60-degree rhombic ribbon.

Furthermore, despite the similarity between the 60-degree rhombic and kagome cell in figure, the topological

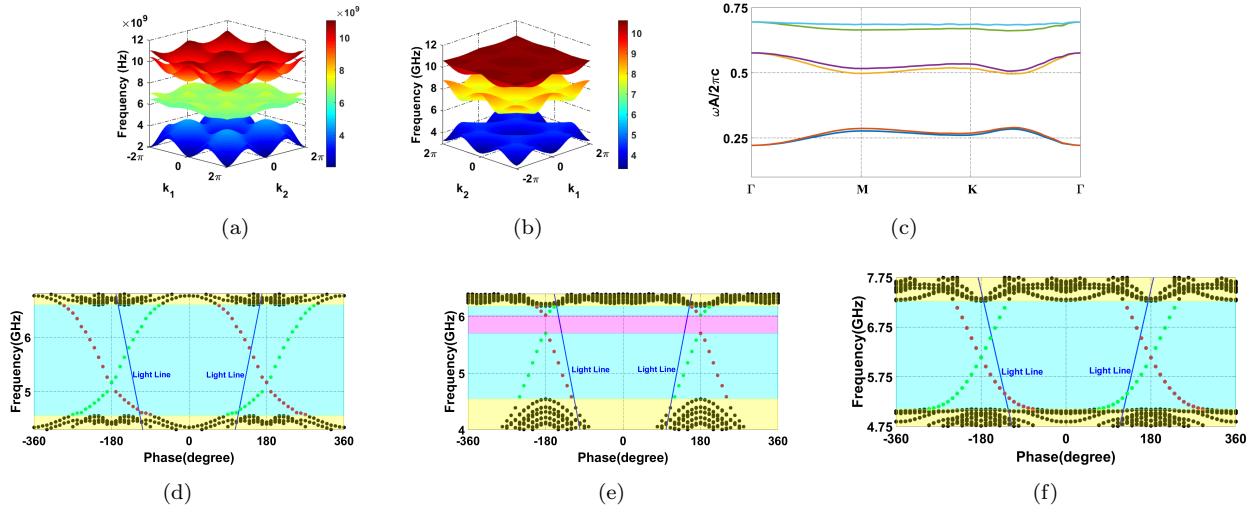


**Fig. 2:** (a) and (b) represent the dispersion diagrams of a 60-degree rhombic and a kagome unit cell displayed in 3D. (c) The IRBZ of the kagome unit cell demonstrates mode degeneracy, which is a necessary condition for being topological. (d)-(f) show the dispersion diagrams for a ribbon designed with three different configurations: a hexagonal unit cell arranged in a zigzag pattern, a 60-degree rhombic unit cell, and a kagome unit cell. The yellow region, marked with black dots, represents the bulk modes, while the cyan region, featuring red and green dots, indicates the edge modes. The differentiation of edge modes into red and green is attributed to the distinction between the two pseudospins. Additionally, the magenta region signifies the gap present in the edge modes. The 60-degree rhombic unit cell features an edge mode that has a bandgap, which is entirely located within the slow wave region. In contrast, the other configurations do not exhibit a bandgap and are suitable for leaky wave antenna applications.

bandgap of the kagome cell is one third more than the 60 degree rhombic cell, approximately, which shows essential differences between them.

Unlike the 60-degree rhombic structure, the kagome structure exhibits no gap in the edge modes, So, a noteworthy advantage of the kagome lattice is its ability to simultaneously facilitate the continuous edge modes characteristic of the honeycomb lattice while also enabling the straight propagation observed in the rhombic lattice. Thus, this metasurface may be a suitable candidate for both guiding wave and leaky wave antenna applications.

To validate the previous results, it is essential to observe the propagation of the edge mode along the interface line by exciting the pseudospins. The pseudospins are excited by a Hertzian dipole, represented by  $E_z + Z_0 H_z$  and  $E_z - Z_0 H_z$ , where  $Z_0$  is the impedance of free space [6].

In the initial step to demonstrate the possibility of robust linear propagation, a pseudospin was excited in the structure depicted in Fig. 3(a), resulting in the robust propagation shown in Fig. 3(b). This represents a significant advantage of the kagome lattice over the hexagonal lattice, as it allows for straight-line propagation, which is not feasible in the hexagonal structure.

To showcase the high degree of freedom and design flexibility of the structure, the shape of the interface line is designed as a Koch snowflake fractal (see Fig. 3(c)). The unidirectional propagation of these pseudospins is illustrated in Figs. 3(d) and 3(e) at a frequency of 5.4 GHz. These observations confirm previous findings and underscore the topological behavior of the kagome structure.

## 2.2 Parametric study

A parametric study is necessary to examine how the dimensions of the cell affect the limits of the topological bandgap. To achieve this, we calculated the dispersion diagram for various values of period length and border width. The results of this parametric study, illustrated in Fig. 4, show that as the period length increases, the bandgap shifts to lower frequencies, and its width decreases. Conversely, increasing the border width results in a widening of the bandgap; however, the rate of increase depends on the period length, as it tends to decrease with longer period lengths.

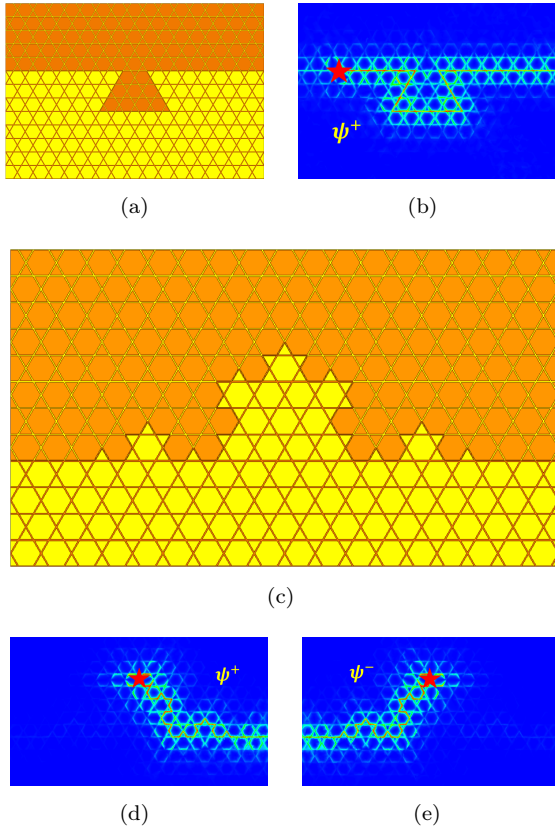


**Fig. 3:** (a) and (b) The structure is arranged in a kagome lattice, demonstrating the possibility for robust linear propagation. (c) The shape of the interface has been changed to a Koch snowflake fractal, highlighting its ability to make sharp turns and its robustness in propagation. (d) and (e) demonstrate the unidirectional propagation of pseudospin up ( $\psi^+$ ) and down ( $\psi^-$ ), respectively. The excitation point is located at the snowflake's apex, marked by a red star.

Based on the results of the parametric study, the period length and border width were selected as 13 mm and 0.625 mm, respectively, to establish the topological bandgap in the X-band frequencies. To confirm that these dimensions achieve the desired frequency band, the dispersion diagram of one cell was calculated and is shown in Fig. 5(a) in a 3D display, which validates the chosen dimensions. Additionally, to analyze the behavior of the edge mode, the dispersion diagram of one ribbon of the structure was obtained and is illustrated in Fig. 5(b). This dispersion diagram resembles that of Fig. 2(f), with some portions of the mode located in the fast wave region, making it suitable for leaky-wave antenna applications.

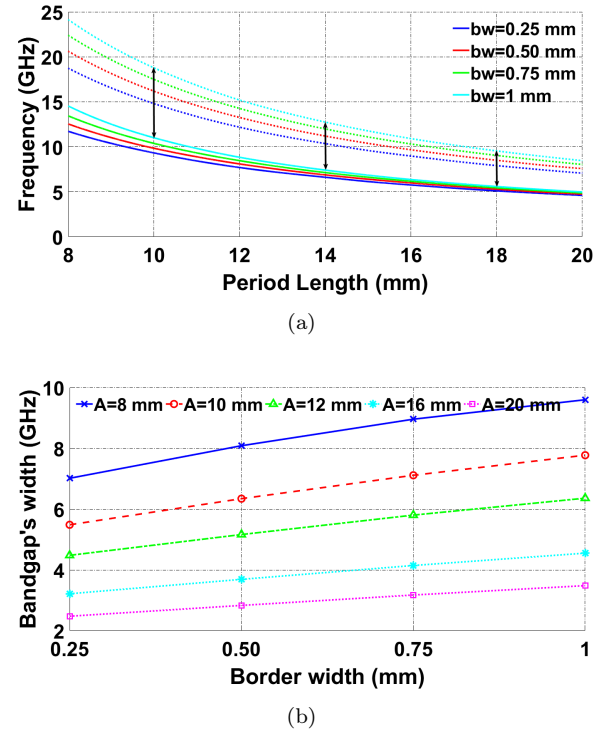


**Fig. 4:** The parametric study of the kagome unit cell regarding period length and border width. (a) The variation of the maximum of the lower band (solid lines) and the minimum of the upper band (dashed lines) with respect to the period length is demonstrated for various border widths. The arrows indicate the reduction in the bandgap width as the period length increases. (b) The variation of bandgap width in relation to border width is illustrated for several periodic lengths. It demonstrates that the width of the bandgap increases with an increase in border width or a decrease in periodic length. However, the impact of increasing the border width diminishes with an increase in the period length.

### 3 Leaky-wave antenna application

Given the robust propagation features of the kagome structure and drawing inspiration from the findings in [21] regarding the armchair arrangement, the interface line has been designed to mimic the armchair configuration. This design is illustrated in Fig.6(a) for a single ribbon. The confinement of the electric field at the interface confirms the accuracy of the calculations. The dispersion diagram for the ribbon, shown in Fig.6(b), reveals the presence of an edge mode similar to that of the hexagonal configuration described in [21]. This edge mode spans the entire bandgap, indicating that this structure can be utilized for a leaky-wave antenna operating throughout the topological bandgap.

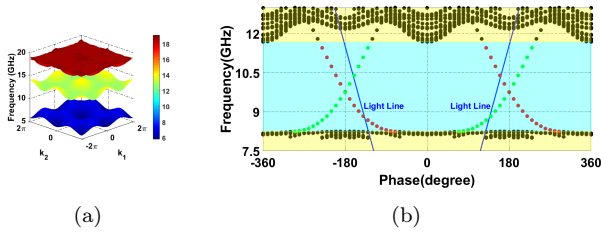


**Fig. 5:** (a) The 3D dispersion diagram of the kagome cell features a 13 mm period length and a border width of 0.625 mm. The substrate used is a 1.57 mm thick Rogers/Duroid 5880. (b) Dispersion diagram for a single ribbon of the kagome structure, based on the specified dimensions, reveals that a portion of the edge mode is situated in the fast wave region, which can be utilized for leaky-wave antenna applications.

This capability will influence the antenna's bandwidth and scanning range.

A critical aspect of the dispersion diagram is the positioning of the edge modes and their spatial harmonics in the fast wave region, indicating the simultaneous propagation of two modes with positive and negative phase velocities. Consequently, radiation can occur in both forward and backward directions, resulting in the relevant leaky-wave antenna generating two beams directed forward and two beams directed backward.

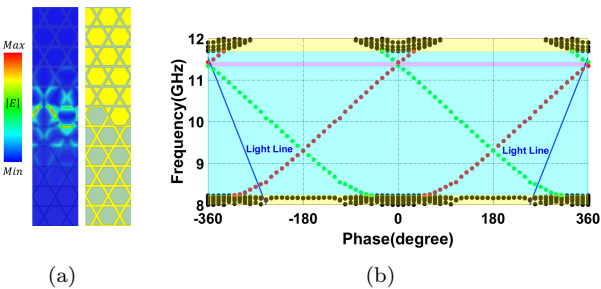


**Fig. 6:** (a) The interface line is similar to the armchair arrangement, and the electric field profile is confined to the interface. (b) The dispersion diagram of the demonstrated kagome structure ribbon in the armchair arrangement shows the presence of two modes in the fast wave region simultaneously. One of these modes exhibits right-hand behavior due to its positive phase velocity, while the other mode displays left-hand behavior, corresponding to its negative phase velocity.

The antenna structure is illustrated in Fig. 7(a) and is coupled to the classical line via the Antipodal Slot Line (ASL), as introduced in [34]. Due to the arm-

chair shape of the interface, the connection between the ASL and the topological structure is analogous to that discussed in [21]. The return and insertion losses of the proposed antenna, simulated using Ansys HFSS and CST Studio, are presented in Fig. 7(b). The results from both simulations are in good agreement, validating the findings. The frequency ranges for the bulk modes and the edge mode bandgap are highlighted in yellow and cyan, respectively.

These results align with the dispersion diagram in Fig.6(b), validating the simulations. Based on these observations, the desired operating frequency range of 8.8-11.1 GHz has been selected to facilitate forward and backward radiation.

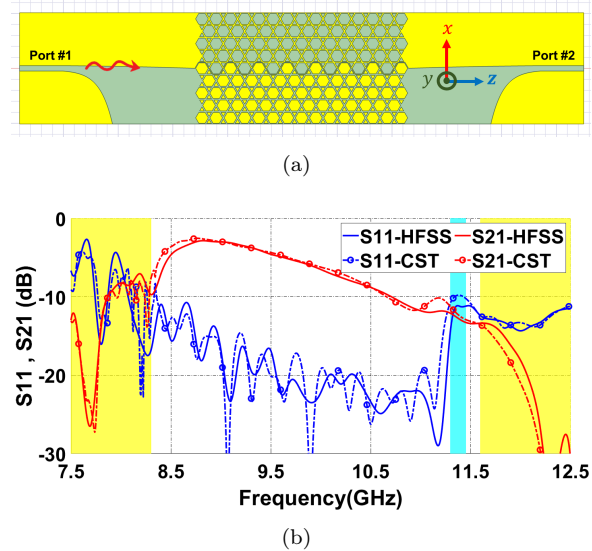


**Fig. 7:** The structure of the proposed leaky wave antenna using a kagome lattice arranged in an armchair configuration is shown in (a). The antenna is excited using an ASL, similar to the approach in [21]. In (b), the return and insertion losses from simulations conducted in Ansys HFSS and CST Studio are presented and aligned, confirming the accuracy of the simulation results. The yellow bands indicate the presence of bulk modes, while the cyan band identifies the gap region in Fig.6(b), where the return loss has increased.

The frequency range of 11.1 to 11.7 GHz cannot be selected, even though it falls within the topological bandgap. This issue arises due to a reduction in the attenuation of bulk modes within that range. To illustrate this problem visually, the electric field profiles within the structure are shown in Fig. 8 for frequencies of 10 GHz and 11.5 GHz. At 10 GHz, the elec-



tric field is confined to the interface line and decreases rapidly through the bulk; however, at 11.5 GHz, the attenuation rate of the bulk modes decreases significantly and cannot be overlooked. These bulk modes would negatively impact the radiation pattern, making it undesirable. Therefore, this frequency range is not operational.

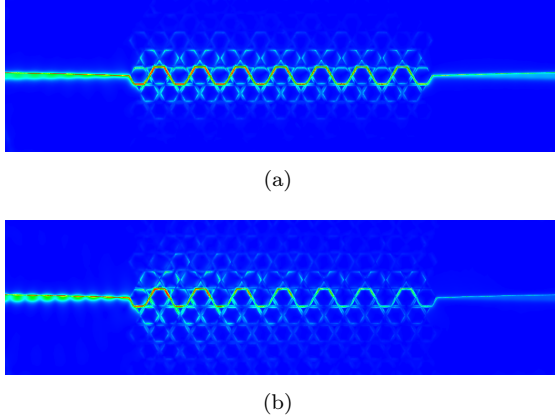


**Fig. 8:** The electrical field profile of the structure at frequencies of 10 GHz ((a)) and 11.5 GHz ((b)) reveals that the attenuation of the bulk modes at 11.5 GHz is significantly lower than at 10 GHz. As a result, the radiation pattern at 11.5 GHz is not acceptable. These findings are consistent with the dispersion diagram shown in Fig.6(b) and the S-parameters illustrated in Fig.7(b), which validate the simulations.

Based on previous results, the radiation pattern of the proposed antenna has been calculated and illustrated in Fig. 9. The 3D display of the realized gain pattern at 11 GHz, shown in Fig. 9(a), demonstrates the antenna's capabilities by providing both forward and backward beams. This aligns with the dispersion diagram presented in Fig. 6(b).

The scanning behavior of the antenna was analyzed using Ansys HFSS and CST Studio, with results presented in Figures 9(b) and (c), respectively. These figures illustrate the realized gain patterns in the plane of  $\phi = 90^\circ$  for frequencies of 8.8 GHz, 10 GHz, and 11 GHz. The backward beams are observed to shift from approximately  $\pm 145^\circ$  to  $\pm 95^\circ$ , while the forward beams shift from about  $\pm 64^\circ$  to  $\pm 17^\circ$ . Consequently, the forward and backward beams exhibit scan ranges of  $50^\circ$  and  $47^\circ$ , respectively. The proximity of these two scan ranges aligns with the edge modes shown in the dispersion diagram of Figure 6(b), thereby confirming these results.

Moreover, to demonstrate the consistency between the simulation results from Ansys HFSS and CST Studio, the realized gain patterns for 8.8 GHz, 10 GHz, and 11.1 GHz are plotted in separate figures: Figures 9(d), (e), and (f), respectively. These plots further validate the simulations.

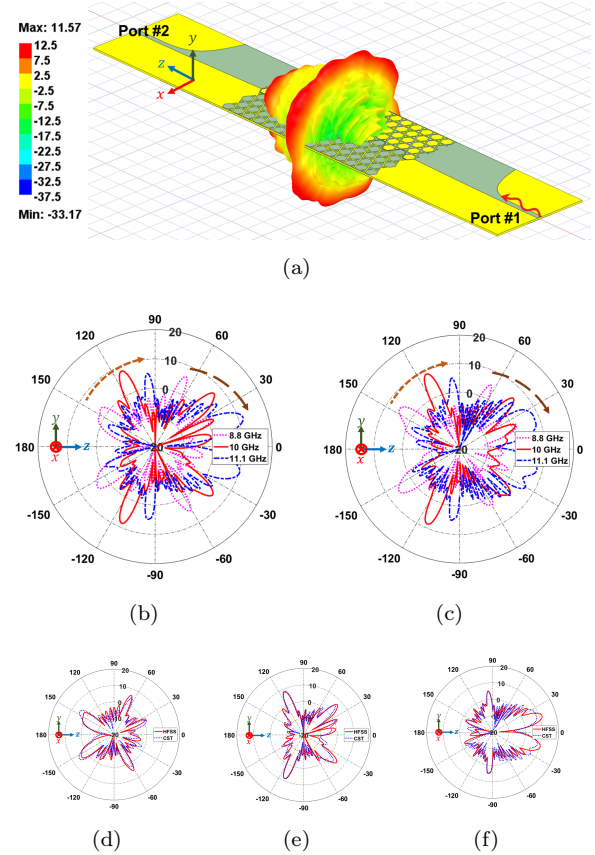


**Fig. 9:** (a) The realized gain pattern of the proposed antenna at 11 GHz shows two beams directed forward and two directed backward. The pair of backward beams is positioned near the broadside, while the forward beams are located close to the end-fire direction. (b) and (c) represent the realized pattern results for  $\phi = 90^\circ$  in Ansys HFSS and CST Studio, respectively, at frequencies of 8.8 GHz, 10 GHz, and 11.1 GHz. The arrows indicate the direction of rotation for the main lobes as the frequency increases. The realized gain of the backward beams initially increases and then decreases with rising frequency, while the realized gain of the forward beams continues to increase consistently. The comparison of results from Ansys HFSS and CST Studio, as shown in figures (d)-(f) for frequencies of 8.8 GHz, 10 GHz, and 11.1 GHz, clearly establishes a strong alignment between the simulations from both software platforms. This robust agreement in the observed patterns decisively confirms the reliability of the results.

An important aspect of the realized gain patterns shown in Fig. 9 is how the realized gain values change for each beam as the frequency increases. Specifically, the realized gain of backward beams initially increases and then decreases as they approach the broadside direction. In contrast, the realized gain of the forward beams continues to rise consistently.

Upon examining the forward beams in Fig. 9(b) or (c), it becomes evident that the realized gain and the half power beam width (HPBW) of the forward beams increase simultaneously with frequency. This phenomenon may appear confusing at first; however, a closer look at the 3D display of the patterns clarifies the situation. The increase in frequency causes the beam to focus more along the azimuthal angle ( $\phi$ ), leading to a greater concentration of energy in the plane at  $\phi = 90^\circ$ . As a result, both the realized gain and HPBW rise.

It's important to note that in such antennas, lower HPBW values observed in a 2D pattern do not necessarily indicate higher directivity or gain. This highlights the significance of presenting the radiation pattern in a 3D display, a detail that is often missing in some research papers.

## 4 conclusion

The article discusses a spin PTI based on a kagome lattice and its unit cell. It presents the dispersion diagram of the unit cell in both its IRBZ and a three-dimensional representation. The results show a 33 percent increase in the topological bandgap compared to the 60-degree rhombic unit cells, even though their shapes are similar. By calculating the dispersion diagram for a single ribbon of the kagome structure, the existence of edge modes within the topological bandgap was confirmed. These modes occur without any gap and are found in both slow and fast wave regions.

To demonstrate robustness, unidirectional propagation of pseudospins, and the ability to make various sharp turns, the interface line is designed in the shape of a Koch snowflake. A parametric study was performed on the period length and border width to determine the optimal dimensions for achieving the topological bandgap in the X-band frequency range. These findings were further validated using the dispersion diagram of the single ribbon.

To apply the kagome lattice in leaky-wave antennas, the interface line was designed in an armchair config-

uration to position most of the edge modes in the fast wave region. This modification ensures that the edge mode and its spatial harmonic are situated in the fast wave region, where they exhibit different and opposite phase velocities. For excitation, the structure is coupled with the classical line through ASL. As a result, the S-parameters demonstrate effective coupling, which aligns with the dispersion diagram of a single ribbon.

The realized gain pattern of the proposed antenna is shown in Fig. 9. It illustrates a scan range of 50 degrees for backward radiation and 47 degrees for forward radiation. Notably, the realized gain and the HPBW of the forward beams increase simultaneously. This trend is attributed to the concentration of the beams around the  $\phi = 90^\circ$  plane. As a result, the HPBW does not provide a clear interpretation of the antenna's gain or directivity.

In Table 1, a comparison is presented among various antennas that are based on different types of PTIs. The proposed antenna in this work features the highest number of beams, resulting in the widest scanning range compared to the others. Notably, this antenna is the only one that can simultaneously provide scanning in both backward and forward directions.

**Acknowledgment:** We would like to thank Prof. A. Zeidaabadi Nezhad from Isfahan University of Technology and Dr. R.J.B. Davis from University of California, San Diego for the fruitful and illuminating discussions.

**Research funding:** This research received no specific grant from any funding agency or university.

**Author contributions:** All authors have accepted responsibility for the entire content of this manuscript and approved its submission.

**Conflict of interest:** Authors state no conflict of interest.

**Data availability statement:** The datasets generated and analyzed during the current study are available from the corresponding author on reasonable request.

Tab. 1: comparison between leaky-wave antennas based on PTIs.

	Type	Lattice Interface shape	Bandwidth	Number of beams	Scanning Range <sup>1</sup>	3D Pattern
[17]	Chern PTI	square Straight	6.34-6.76 GHz	1	$\approx 70^\circ$ to $110^\circ$	×
[35]	Chern PTI	square Straight	13.2-14 GHz	1	$\approx 52^\circ$ to $40^\circ$	×
[20]	Valley PTI	Hexagonal Even-mode	8.2-8.7 GHz	1	$\approx 105^\circ$ to $80^\circ$	✓
[19]	Spin PTI	Hexagonal Zig-Zag	19.75-21.25 GHz	2	$\pm 166^\circ$ to $\pm 130^\circ$	×
[11]	Spin PTI	$30^\circ$ Rhombic Straight	17.5-20 GHz	2	$\pm 122^\circ$ to $\pm 99.5^\circ$	✓
[21]	Spin PTI	Hexagonal Armchair	8.1-10.8 GHz	2	$\pm 126^\circ$ to $\pm 73^\circ$	✓
This work	Spin PTI	Kagome Armchair	8.8-11.1 GHz	4	Backward : $\pm 145^\circ$ to $\pm 95^\circ$ Forward : $\pm 64^\circ$ to $\pm 17^\circ$	✓

<sup>1</sup> The broadside is at  $90^\circ$

## References

- [1] A. Grbic and S. Maci, "Em metasurfaces [guest editorial]," *IEEE Antennas and Propagation Magazine*, vol. 64, no. 4, pp. 16–22, 2022.
- [2] R. Davis, Y. Zhou, P. Bandaru, D. Sievenpiper *et al.*, "Photonic topological insulators: A beginner's introduction [electromagnetic perspectives]," *IEEE Antennas and Propagation Magazine*, vol. 63, no. 3, pp. 112–124, 2021.
- [3] Z. Wang, Y. Chong, J. D. Joannopoulos, and M. Soljačić, "Observation of unidirectional backscattering-immune topological electromagnetic states," *Nature*, vol. 461, no. 7265, pp. 772–775, 2009.
- [4] Y. Poo, R.-x. Wu, Z. Lin, Y. Yang, and C. T. Chan, "Experimental realization of self-guiding unidirectional electromagnetic edge states," *Physical Review Letters*, vol. 106, no. 9, p. 093903, 2011.
- [5] J. B. Dia'aaldin and D. F. Sievenpiper, "Topological metasurfaces for symmetry-protected electromagnetic line waves," in *Metamaterials, Metadevices, and Metasystems 2019*, vol. 11080. SPIE, 2019, pp. 20–26.
- [6] D. J. Bisharat and D. F. Sievenpiper, "Electromagnetic-dual metasurfaces for topological states along a 1d interface," *Laser & Photonics Reviews*, vol. 13, no. 10, p. 1900126, 2019.
- [7] T. Ozawa, H. M. Price, A. Amo, N. Goldman, M. Hafezi, L. Lu, M. C. Rechtsman, D. Schuster, J. Simon, O. Zilberberg *et al.*, "Topological photonics," *Reviews of Modern Physics*, vol. 91, no. 1, p. 015006, 2019.
- [8] R. J. B. Davis, *Topological Physics in Real and Reciprocal Space: Investigations in Electromagnetics*. University of California, San Diego, 2023.
- [9] A. B. Khanikaev, S. Hossein Mousavi, W.-K. Tse, M. Kargarian, A. H. MacDonald, and G. Shvets, "Photonic topological insulators," *Nature materials*, vol. 12, no. 3, pp. 233–239, 2013.
- [10] R. J. Davis and D. F. Sievenpiper, "Robust microwave transport via nontrivial duality-based rhombic unit cells," in *2021 IEEE International Symposium on Antennas and Propagation and USNC-URSI Radio Science Meeting (APS/URSI)*. IEEE, 2021, pp. 619–620.
- [11] S. Ahmad Abtahi, M. Maddahali, and A. Bakhtafrouz, "Realizable leaky wave antenna based on spin photonic topological insulators," *IEEE Access*, vol. 12, pp. 152 850–152 859, 2024.
- [12] Z. Xu, J. Chang, S. Fang, Q. Zhang, R. J. Davis, D. Sievenpiper, and T. J. Cui, "Line waves existing at junctions of dual-impedance metasurfaces," *ACS Photonics*, vol. 8, no. 8, pp. 2285–2293, 2021.
- [13] M. SalarRahimi and G. A. Vandenbosch, "Exciting the edge mode in a dual metasurface ptd symmetric waveguide," in



- 2020 4th Australian Microwave Symposium (AMS). IEEE, 2020, pp. 1–2.
- [14] M. Khodadadi, H. Taghvaei, G. Gradoni, and M. Khalily, “Dual and complementary-impedance metasurfaces for enhanced line waves,” in *2024 IEEE International Symposium on Antennas and Propagation and ITNC-USNC-URSI Radio Science Meeting (IEEE AP-S/URSI 2024)*.
- [15] H. Ahmadi and A. Khavasi, “Babinet-complementary structures for implementation of pseudospin-polarized waveguides,” *Optics Express*, vol. 31, no. 13, pp. 21 626–21 640, 2023.
- [16] S. Singh, R. J. Davis, J. B. Dia'aalidin, J. Lee, S. M. Kandil, E. Wen, X. Yang, Y. Zhou, P. R. Bandaru, and D. F. Sievenpiper, “Advances in metasurfaces: Topology, chirality, patterning, and time modulation,” *IEEE Antennas and Propagation Magazine*, vol. 64, no. 4, pp. 51–62, 2021.
- [17] Z. Xu, M. Wang, S. Fang, H. Liu, Z. Wang, and D. F. Sievenpiper, “Broadside radiation from chern photonic topological insulators,” *IEEE Transactions on Antennas and Propagation*, vol. 70, no. 3, pp. 2358–2363, 2021.
- [18] J. Han, F. Liang, D. Huang, Y. Zhao, J. Liu, D. Zhao, and B.-Z. Wang, “Topological traveling-wave radiation based on chiral edge states in photonic chern insulators,” *Opt. Lett.*, vol. 49, no. 21, pp. 6233–6236, Nov 2024. [Online]. Available: <https://opg.optica.org/ol/abstract.cfm?URI=ol-49-21-6233>
- [19] S. Singh, D. Bisharat, and D. Sievenpiper, “Topological antennas: Aperture radiators, leaky-wave surfaces, and orbital angular momentum beam generation,” *Journal of Applied Physics*, vol. 130, no. 2, p. 023101, 2021.
- [20] Z. Xu, X. Sun, H. Wu, Z. Xiong, X. Zhou, H. Yu, X. Yin, D. F. Sievenpiper, and T. J. Cui, “Terminal-matched topological photonic substrate-integrated waveguides and antennas for microwave systems,” *Advanced Science*, vol. 11, no. 33, p. 2404163, 2024. [Online]. Available: <https://onlinelibrary.wiley.com/doi/abs/10.1002/advs.202404163>
- [21] S. A. Abtahi, M. Maddahali, and A. Bakhtafrouz, “Spin photonic topological insulator antenna by armchair arrangement,” *arXiv e-prints*, pp. arXiv-2411, 2024.
- [22] Q. Wang, H. Lei, Y. Qi, and C. Felsler, “Topological quantum materials with kagome lattice,” *Accounts of Materials Research*, vol. 5, no. 7, pp. 786–796, 2024.
- [23] J.-X. Yin, B. Lian, and M. Z. Hasan, “Topological kagome magnets and superconductors,” *Nature*, vol. 612, no. 7941, pp. 647–657, 2022.
- [24] H.-M. Guo and M. Franz, “Topological insulator on the kagome lattice,” *Phys. Rev. B*, vol. 80, p. 113102, Sep 2009.
- [25] L. Zhang, “Valley-hall-like second-order photonic topological insulators in kagome lattice.” *arXiv: Optics*, 2019.
- [26] H. Zhong, R. Wang, F. Ye, J. Zhang, L. Zhang, Y. Zhang, M. R. Belić, and Y. Zhang, “Topological insulator properties of photonic kagome helical waveguide arrays,” *Results in Physics*, 2019.
- [27] S. Wong, M. Saba, O. Hess, and S. S. Oh, “Photonic topological insulator edge modes using all-dielectric kagome photonic crystals,” *2019 Thirteenth International Congress on Artificial Materials for Novel Wave Phenomena (Metamaterials)*, pp. X-471–X-473, 2019.
- [28] D. Leykam and D. A. Smirnova, “Probing bulk topological invariants using leaky photonic lattices,” *Nature Physics*, vol. 17, pp. 632 – 638, 2020.
- [29] H. Li, C. Luo, T. Zhang, J. Xu, X. Zhou, Y. Shen, and X. Deng, “Topological refraction in kagome split-ring photonic insulators,” *Nanomaterials*, vol. 12, 2021.
- [30] Y. He, Y. Gao, Y. He, X.-F. Qi, J. Si, M.-K. Yang, and S. Zhou, “Realization of edge and corner states in photonic crystals with kagome lattices through topological insulator generators,” *SSRN Electronic Journal*, 2022.
- [31] Y. Gao, Y. He, J. Si, S. Rouzi, M.-C. Jin, Y. He, and M. Yang, “Waveguide–cavity coupling system based on topological edge states and corner states in kagome photonic crystals,” *Advanced Quantum Technologies*, vol. 7, 2023.
- [32] B.-U. Sohn, J. W. Choi, G. F. Chen, H. Gao, W. J. Mitchell, D. K. T. Ng, and D. T. H. Tan, “Topologically protected parametric wavelength conversion in a valley hall insulator,” *Laser & Photonics Reviews*, 2024.
- [33] J. Haegeman, V. Zauner, N. Schuch, and F. Verstraete, “Shadows of anyons and the entanglement structure of topological phases,” *Nature communications*, vol. 6, no. 1, p. 8284, 2015.
- [34] R. J. Davis, D. J. Bisharat, and D. F. Sievenpiper, “Classical-to-topological transmission line couplers,” *Applied Physics Letters*, vol. 118, no. 13, p. 131102, 2021.
- [35] J. Han, F. Liang, D. Huang, Y. Zhao, J. Liu, D. Zhao, and B.-Z. Wang, “Topological traveling-wave radiation based on chiral edge states in photonic chern insulators,” *Opt. Lett.*, vol. 49, no. 21, pp. 6233–6236, Nov 2024. [Online]. Available: <https://opg.optica.org/ol/abstract.cfm?URI=ol-49-21-6233>